V2G Control Strategy for Single-Phase Matrix Converter-Based WPT System to Suppress Grid Current Harmonics

Yuchen Wei, Wei Liu, *Senior Member*, *IEEE*, Fengjiang Wu, *Senior Member*, *IEEE*, Chang Liu, K. T. Chau, *Fellow*, *IEEE*

Abstract: **The bidirectional power transfer capability of matrix converter-based wireless power transfer (WPT) systems renders them suitable for vehicle-to-grid (V2G) applications. However, grid voltage harmonics induce severe grid current distortion, which limits their practical applicability. In this paper, a linearized model of the matrix converter-based WPT system under V2G operation is established. Based on this, the impact of grid voltage harmonics on grid current harmonics is analyzed. To address this issue, a composite control architecture integrating grid voltage feedforward compensation and grid current feedback regulation is proposed. Building upon this architecture, a proportional-resonant composite iterative learning controller is developed for closed-loop current control. The parameters of both the feedforward and closed-loop controllers are designed to ensure system stability and enhance harmonic suppression. Finally, the feasibility of the proposed method is verified through experimental verification.**

Item index: **Wireless power transfer, vehicle-to-grid, harmonic suppression, control strategy.**

I. Introduction

Wireless power transfer (WPT) technology [1-3] holds great promise in the field of electric vehicle (EV) charging [4-7]. It has several advantages, including contactless operation, high automation, and strong environmental adaptability. Bidirectional WPT technology further enables vehicle-to-grid (V2G) operation. EVs are transformed from passive electricity consumers into mobile energy storage units. These units can participate in peak shaving, grid frequency regulation, and voltage stabilization [8, 9].

The key to achieving V2G lies in constructing a power conversion system capable of bidirectional AC-DC conversion [10]. This requirement inherently eliminates all topologies based on diode rectifiers, which support only unidirectional power flow [11, 12]. Currently, bidirectional WPT systems typically adopt active full-bridge converters on the EV battery side. On the grid side, a two-stage topology is usually employed, consisting of a low-frequency full-bridge rectifier cascaded with a high-frequency full-bridge inverter [13-15]. However, the two-stage topology involves an intermediate DC bus and large electrolytic capacitors, increasing the system volume and significantly reducing the lifespan. Moreover, the cascaded nature of the two-stage topology reduces the system stability margin [16].

Matrix converters (MC) are highly suitable for V2G applications, due to their capability of direct and bidirectional conversion from low-frequency AC to high-frequency AC [17-19]. MC-based WPT systems eliminate the intermediate DC link and bulky electrolytic capacitors. This greatly improves system power density and operational lifespan, addressing the issues associated with conventional two-stage topologies. With the advent of integrated bidirectional SiCs and GaNs [20], the number of power switches required in MC can be halved. This significantly reduces hardware costs and further enhances power density and efficiency in WPT systems.

To ensure stable energy exchange between the grid and EVs, control strategies for bidirectional WPT systems are also important. Current research primarily focuses on accurate power flow regulation [21-22] and unity power factor control [23]. Control strategies based on phase-shift modulation combined with phase synchronization are widely verified to support switching between V2G and grid-to-vehicle (G2V) modes [19]. By introducing control variables such as primary-side phase shift, secondary-side phase shift, and the phase delay between the two, the active and reactive power regulation is achieved [21]. It maintains unity power factor operation and significantly reduces harmonic content in the system.

However, existing V2G control strategies [21-23] are generally based on the assumption of an ideal sinusoidal grid voltage and fail to consider the impact of grid voltage harmonics on system performance. In practical grid conditions, voltage distortion becomes a non-negligible issue [24]. Harmonics in grid voltage lead to increased grid current harmonics on the output side of the WPT system. This degrades power factor, increases system losses, and worsens grid pollution. Conventional PI and PR controllers lack sufficient gain at harmonic frequencies, resulting in poor harmonic suppression capability [25]. Therefore, under non-ideal grid conditions, how to effectively suppress harmonic components in the grid current is a key technical challenge hindering the further development of WPT V2G applications.

To address the above issues, this paper proposes a V2G control strategy for the MC-based WPT system aimed at suppressing grid current harmonics under distorted grid

This work was supported in part by the Hong Kong Research Grants Council, Hong Kong Special Administrative Region, China, under Grant T23-701/20-R, and in part by The Hong Kong Polytechnic University under Grants P0048560, P0048360, and P0054038. (*Corresponding author: K.T. Chau.*)

Yuchen Wei, Wei Liu, Chang Liu and K.T. Chau are with the Research Centre for Electric Vehicles and Department of Electrical and Electronic Engineering, The Hong Kong Polytechnic University, Hong Kong, China (e-mail: yuchen.wei@polyu.edu.hk; wei.liu@polyu.edu.hk; coeng.liu@connect.polyu.hk; k.t.chau@polyu.edu.hk).

Fengjiang Wu is with the School of Electrical Engineering, Harbin Institute of Technology, China (e-mail: shimeng@hit.edu.cn).

conditions. The innovations and contributions of this paper are as follows. (1) A linearized model of the MC-based WPT system under V2G operation is established, enabling a clear analysis of the impact of grid voltage harmonics on grid current distortion. (2) A composite control architecture integrating grid voltage feedforward compensation and grid current closed-loop regulation is proposed to mitigate the effect of voltage harmonics. (3) A proportional-resonant composite iterative learning controller is proposed to further suppress grid current harmonics. (4) Based on the built model, the design process of the proposed composite controller is presented to improve the stability margin and transient performance.

II. Operation Principle of MC-Based WPT System Under V2G Operation

The topology of the MC-based WPT system is shown in Fig. 1. Owing to the bidirectional power transfer capability of the full-bridge inverter and MC, the system can operate in both G2V and V2G modes. While the G2V operation in MC-WPT systems is extensively researched [17-19], this paper focuses on the V2G operation, particularly improving its grid current quality. By the inverter (S_1-S_4), the DC voltage (U_b) of the EV battery is converted to a high-frequency voltage (u_{ab}). Through the series-to-series (S-S) network and coils, the power is transmitted wirelessly from the primary side to the secondary side. On the secondary side, the high-frequency AC voltage (u_{cd}) is directly converted to the low-frequency AC voltage by the matrix converter (Q_1-Q_4). Through the grid filter, the power is delivered to the grid, and the V2G operation is achieved.

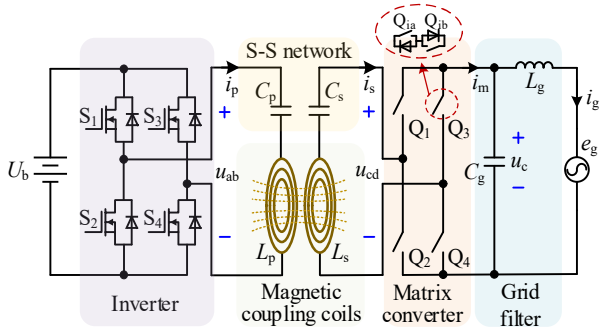

Fig. 1. Topology of single-phase MC-based WPT system under V2G operation.

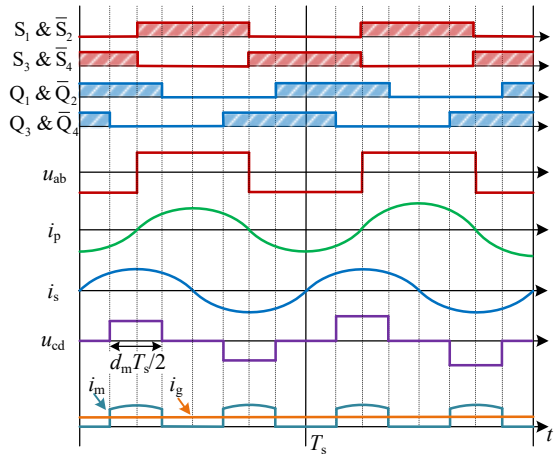

Fig. 2. Key waveforms of MC-based WPT system under V2G operation.

In Fig. 1, i_p and i_s are the primary and secondary coil currents, respectively. i_m is the MC output current, and i_g is the grid current. u_c is the filter capacitor voltage. e_g is the grid voltage. In an ideal grid, $e_g=U_g\sin(\omega_1 t)$. U_g represents the grid voltage amplitude, and ω_1 represents the grid fundamental angular frequency. The fundamental RMS values of u_{ab}, u_{cd}, i_p, and i_s are represented by U_{ab}, U_{cd}, I_p, and I_s, respectively.

The key operation waveforms under the V2G operation are shown in Fig. 2. On the primary side, the phase-shift modulation is adopted to adjust the inverter. The duty cycle ratio is set as 1, and the waveform of u_{ab} is a square wave. The fundamental RMS value of u_{ab} is expressed as

$$U_{ab}=\frac{2\sqrt{2}}{\pi}U_b \tag{1}$$

Then, the power is transmitted from the primary side to the secondary side through the S-S network. According to the steady-state characteristic of the S-S network under the resonant state, the RMS value of the secondary coil current is derived as

$$I_s=\frac{U_{ab}}{\omega_r M}=\frac{2\sqrt{2}U_b}{\pi\omega_r M} \tag{2}$$

where ω_r is the resonant angular frequency. M is the mutual inductance of the magnetic coupling coils.

On the secondary side, the MC is also controlled by the phase-shift modulation. By adjusting the duty cycle ratio of MC ($0\le d_m\le 1$), the average value of the MC output current (I_m) at a switching cycle is controlled as

$$I_m=\frac{2\sqrt{2}}{\pi}I_s\sin(\frac{\pi}{2}d_m)\operatorname{sgn}(u_C) \tag{3}$$

Since the time constant of the grid filter is small, $u_c\approx e_g$, and $I_m\approx i_g$ under the ideal grid. Therefore, the grid current is controlled by adjusting d_m. To ensure the high quality of the grid current, i_g should be controlled as $I_g^*\sin(\omega_1 t)$. I_g^* is the desired amplitude of the grid current. According to (2) and (3), d_m under the ideal grid is derived as

$$d_{m\_ideal}=\frac{2}{\pi}\arcsin\left[\frac{\pi^2\omega_r M I_g^*\left|\sin(\omega_1 t)\right|}{8U_b}\right] \tag{4}$$

By adjusting d_m according to (4), the grid current can be shaped into a sinusoidal waveform that is in phase with the grid voltage under ideal grid conditions.

III. Modeling and Characteristic Analysis Under Grid Harmonics Condition

In practical grids, odd-order harmonics are commonly present in the grid voltage, which adversely affects the quality of the grid current. In this section, the model of the MC-based WPT system under V2G operation is built. Based on this, the grid current characteristics under the grid voltage harmonics are analyzed to provide the theoretical basis for the solution method.

In the MC-based WPT system, the MC duty cycle ratio d_m is the control variable, and the non-ideal grid voltage with harmonics is the perturbation variable. To analyze the system behavior, the transfer functions from both the MC duty cycle ratio and the grid voltage to the grid current must be derived through system modeling.

The overall model of the MC-based WPT system consists of four parts, including the primary inverter, S-S resonant network, secondary MC, and grid filter. The inverter model

is given in (1). The other three parts are derived as follows.

First, the model of the S-S resonant network is built. According to the extended description function method [26], the transfer function from U_{cd} to I_s is derived as

$$G_{Ucd-Is}=\frac{I_s}{U_{cd}}=C\left(sI-A\right)^{-1}B \tag{5}$$

$$A=\begin{bmatrix}
\frac{L_s}{\Delta}R_p & \omega_r & \frac{L_s}{\Delta} & 0 & \frac{M}{\Delta}\left(R_s+R_{ac}\right) & 0 & \frac{M}{\Delta} & 0\\
-\omega_r & \frac{L_s}{\Delta}R_p & 0 & \frac{L_s}{\Delta} & 0 & \frac{M}{\Delta}R_s & 0 & \frac{M}{\Delta}\\
\frac{1}{C_p} & 0 & 0 & \omega_r & 0 & 0 & 0 & 0\\
0 & \frac{1}{C_p} & -\omega_r & 0 & 0 & 0 & 0 & 0\\
\frac{M}{\Delta}R_p & 0 & \frac{M}{\Delta} & 0 & \frac{L_p}{\Delta}\left(R_s+R_{ac}\right) & \omega_r & \frac{L_p}{\Delta} & 0\\
0 & \frac{M}{\Delta}R_p & 0 & \frac{M}{\Delta} & -\omega_r & \frac{L_p}{\Delta}R_s & 0 & \frac{L_p}{\Delta}\\
0 & 0 & 0 & 0 & \frac{1}{C_s} & 0 & 0 & \omega_r\\
0 & 0 & 0 & 0 & 0 & \frac{1}{C_s} & -\omega_r & 0
\end{bmatrix} \tag{6}$$

$$B=\begin{bmatrix}0 & \frac{M}{\Delta} & 0 & 0 & 0 & \frac{L_p}{\Delta} & 0 & 0\end{bmatrix}^T \tag{7}$$

$$C=\begin{bmatrix}0 & 0 & 0 & 0 & 0 & 1 & 0 & 0\end{bmatrix} \tag{8}$$

where R_p and R_s are the parasitic resistances of the primary and secondary coils, respectively. $R_{ac}=8U_g/(\pi^2 I_g^*)$ is the AC equivalent resistance of the load. $\Delta=M^2-L_pL_s$. ω_r is the resonant angular frequency.

Next, the model of the single-phase MC is derived as

$$U_{cd}=\frac{2\sqrt{2}}{\pi}\left|u_C\right|\sin(\frac{\pi}{2}d_m) \tag{9}$$

Then, the state equations of the grid filter are derived as

$$\begin{cases}\dfrac{di_g}{dt}=\dfrac{1}{L_g}u_c-\dfrac{1}{L_g}e_g-\dfrac{R_g}{L_g}i_g\\[2ex] \dfrac{du_c}{dt}=\dfrac{1}{C_g}i_m-\dfrac{1}{C_g}i_g\end{cases} \tag{10}$$

From (3), (5), (9) and (10), the large-signal model is built, as shown in Fig. 3(a). Since $|u_c|\times\mathrm{sgn}(u_c)=u_c$, the links of the absolute value function (ABS) and sgn(u_c) are canceled. Due to the nonlinearization of $t_1=(2\sqrt{2}/\pi)I_s\sin(\pi d_m/2)$ and $t_2=(2\sqrt{2}/\pi)u_c\sin(\pi d_m/2)$, this large-signal model is nonlinear and difficult to analyze. To linearize the state equations, the small-signal perturbations are introduced as

$$\begin{cases}\hat{t}_1=\left[\dfrac{2\sqrt{2}}{\pi}\sin(\dfrac{\pi}{2}D_{m\_r})\hat{I}_s+\sqrt{2}I_{s\_r}\cos(\dfrac{\pi}{2}D_{m\_r})\hat{d}_m\right]\\[2ex] \hat{t}_2=\left[\dfrac{2\sqrt{2}}{\pi}\sin(\dfrac{\pi}{2}D_{m\_r})\hat{u}_c+\sqrt{2}U_{c\_r}\cos(\dfrac{\pi}{2}D_{m\_r})\hat{d}_m\right]\end{cases} \tag{11}$$

where $\hat{t}_1$, $\hat{t}_2$, $\hat{d}_m$, $\hat{u}_c$, and $\hat{I}_s$ are the small-signal perturbations of t_1, t_2, d_m, u_c, and I_s, respectively. D_{m_r}, U_{c_r}, and I_{s_r} are the steady-state values of d_m, u_c, and I_s, respectively.

According to (5), (10), and (11), the small-signal model is derived as Fig. 3(b). The perturbation of the grid current is further derived as

$$\begin{cases}\hat{i}_g=G_{dm-ig}\hat{d}_m+G_{eg-ig}\hat{e}_g\\[2ex] G_{dm-ig}=\dfrac{\hat{i}_g}{\hat{d}_m}=\dfrac{\sqrt{2}I_{s\_r}\cos\left(\pi D_{m\_r}/2\right)+2U_{c\_r}\sin\left(\pi D_{m\_r}\right)G_{Ucd-Is}/\pi}{1+\left(L_gs+R_g\right)\left[C_gs+8\sin^2\left(\pi D_{m\_r}/2\right)G_{Ucd-Is}/\pi^2\right]}\\[2ex] G_{eg-ig}=\dfrac{\hat{i}_g}{\hat{e}_g}=-\dfrac{C_gs+8\sin^2\left(\pi D_{m\_r}/2\right)G_{Ucd-Is}/\pi^2}{1+\left(L_gs+R_g\right)\left[C_gs+8\sin^2\left(\pi D_{m\_r}/2\right)G_{Ucd-Is}/\pi^2\right]}\end{cases} \tag{12}$$

where $G_{dm\text{-}ig}$ and $G_{eg\text{-}ig}$ are the transfer functions from d_m and e_g to i_g, respectively.

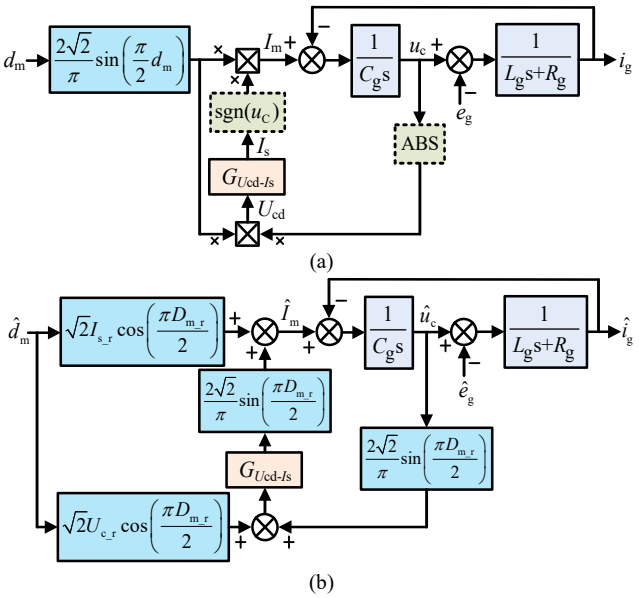

Fig. 3. State space model of MC-based WPT system. (a) Large-signal model. (b) Small-signal model.

Based on the built model, the effect of the grid voltage harmonics on the grid current can be analyzed. The grid voltage with the $2i$+1th order harmonics is expressed as

$$e_g=U_{g1}\sin\left(\omega_1t\right)+U_{g3}\sin\left(\omega_3t\right)+\ldots+U_{g(2i+1)}\sin\left(\omega_{2i+1}t\right) \tag{13}$$

According to (12) and (13), the harmonic components of the grid current are derived as

$$i_{g(2i+1)}=\left|G_{eg-ig}(j\omega_{2i+1})\right|U_{g(2i+1)}\sin\left(\omega_{2i+1}t+\angle G_{eg-ig}(j\omega_{2i+1})\right) \tag{14}$$

Based on (14), the effect of the grid voltage harmonics on the grid current harmonics is shown in Fig. 4.

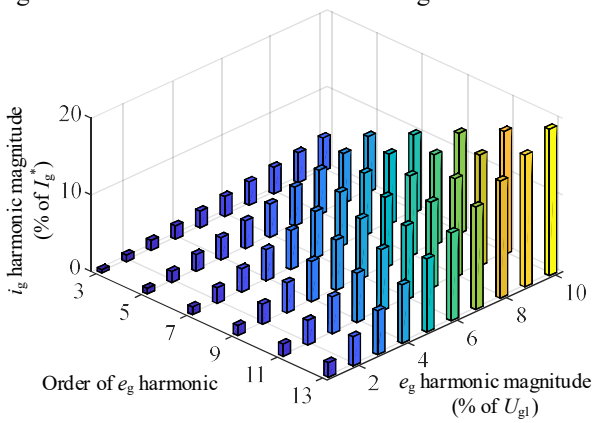

Fig. 4. Effect of grid voltage harmonics on grid current.

As the harmonic order and amplitude of the grid voltage increase, the corresponding harmonic amplitudes in the grid current rise accordingly. For instance, when the grid voltage contains 10% 3rd, 5% 5th, and 5% 7th harmonics, the resulting grid current exhibits 4.34% 3rd, 3.62% 5th, and 5.08% 7th harmonics, respectively. The total harmonic distortion (THD) of the grid current reaches 7.6%. This exceeds the acceptable limits defined by grid standards and thus limits the applicability of the MC-based WPT system in V2G scenarios.

IV. Proposed Closed-Loop Control Strategy

To improve grid current quality under distorted grid voltage conditions, an advanced control strategy must be employed. The conventional PI and PR controllers exhibit limited gains at harmonic frequency points [25], and thus cannot suppress harmonics. In this section, a dual-aspect optimization approach focusing on both control architecture and closed-loop controller is researched. On this basis, the controller parameters are designed to ensure system stability and enhanced harmonic suppression capability.

A. Configuration of Closed-Loop Control System

The block diagram of the proposed closed-loop control strategy is shown in Fig. 5. Since the bandwidth of the closed-loop control system is much lower than the control frequency, the control delay is neglected to facilitate the analysis. The proposed control strategy consists of two parts, namely the feedforward control (FC) of the grid voltage and the closed-loop control of grid current.

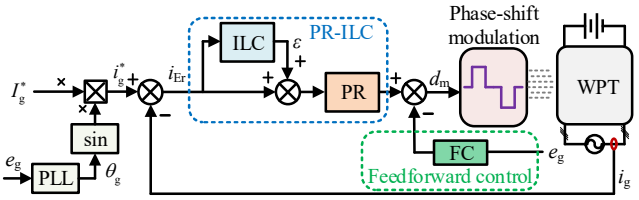

Fig. 5. Block diagram of proposed closed-loop control strategy.

First, the feedforward control of the grid voltage is used to mitigate the adverse impact of voltage harmonics on the grid current. According to Fig. 3(b) and (12), the harmonic components of grid voltage act as the system disturbances, as shown in Fig. 6(a). From Fig. 15(a), the grid voltage harmonics affect this system via the transfer path $G_{eg\text{-}ig}$. Therefore, a feedforward branch of $-G_{eg\text{-}ig}$ can be added to counteract the disturbance. According to the classical control theory, the resulting block diagram is equivalent to Fig. 6(b), effectively achieving harmonic disturbance rejection through feedforward compensation. The detailed structure and parameter design method of the feedforward controller are presented in Section IV-B.

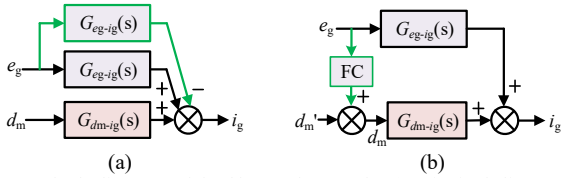

Fig. 6. Block diagram of feedforward control. (a) Principal diagram. (b) Equivalent diagram.

Since feedforward control is inherently open-loop and lacks robustness, it is complemented by a closed-loop grid current controller. To achieve the zero steady-state error tracking and further suppress grid current distortion, a proportional-resonant composite iterative learning controller (PR-ILC) is proposed as shown in Fig. 5.

The PR controller is used to realize the zero steady-state error control of the fundamental current. The discrete domain expression of the PR controller is expressed as

$$G_{\mathrm{PR}}(\mathrm{z}) = K_{\mathrm{p}} + \frac{4K_{\mathrm{r}}T_{\mathrm{sa}}\omega_{\mathrm{c}}(\mathrm{z}^2-1)}{4(\mathrm{z}-1)^2 + 4\omega_{\mathrm{c}}T_{\mathrm{sa}}(\mathrm{z}^2-1) + \omega_{\mathrm{l}}^2 T_{\mathrm{sa}}^2(\mathrm{z}+1)^2} \quad (15)$$

where K_{p} and K_{r} denote the proportional and resonant gains, respectively. ω_{c} is the resonant cutoff frequency. T_{sa} is the sample period. They will be designed in Section IV-C.

The ILC can effectively suppress periodic disturbance signals. Therefore, building upon the PR controller framework, the ILC is embedded to achieve grid current suppression. The output of the ILC is used as the compensation value, and it is summed with the grid current error as the input of the PR controller. The block diagram of the ILC is shown in Fig. 7. The iterative learning law and discrete-domain transfer function are expressed as

$$\varepsilon(k+1) = (1-\Lambda)\varepsilon(k) + \gamma i_{\mathrm{Er}}(k) + \zeta i_{\mathrm{Er}}(k+1) \quad (16)$$

$$G_{\mathrm{ILC}}(\mathrm{z}) = \frac{\zeta \mathrm{z} + \gamma}{\mathrm{z} - 1 + \Lambda} \quad (17)$$

where Λ is the forgetting factor, and γ and ζ are the iterative learning gains. They are greater than zero and less than one. i_{Er} is the current deviation. ε is the ILC output.

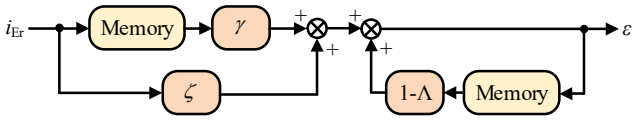

Fig. 7. Block diagram of ILC.

Through the combination of feedforward compensation and PR-ILC-based closed-loop control, the proposed strategy achieves dual-stage suppression of grid current harmonics, ensuring robust and precise current regulation under distorted grid conditions.

B. Design of Feedforward Controller

In this section, the structure and parameter design of the feedforward controller are presented.

From Fig. 6, the transfer function of the feedforward controller is derived as

$$G_{\mathrm{FC}}(\mathrm{s}) = -\frac{G_{eg-ig}(\mathrm{s})}{G_{dm-ig}(\mathrm{s})} \quad (18)$$

where $G_{dm\text{-}ig}$ and $G_{eg\text{-}ig}$ are derived from (12). By substituting (12) into (18), G_{FC} is derived as

$$G_{\mathrm{FC}}(\mathrm{s}) = \frac{C_{\mathrm{g}}\mathrm{s} + 8\sin^2\left(\pi D_{\mathrm{m\_r}}/2\right)G_{U\mathrm{cd}-Is}(\mathrm{s})/\pi^2}{\sqrt{2}I_{\mathrm{s\_r}}\cos\left(\pi D_{\mathrm{m\_r}}/2\right) + 2U_{\mathrm{c\_r}}\sin\left(\pi D_{\mathrm{m\_r}}\right)G_{U\mathrm{cd}-Is}(\mathrm{s})/\pi} \quad (19)$$

As derived in (19), the order of the feedforward controller G_{FC} is eight. Such a high-order controller is challenging to implement on a digital signal processor (DSP) due to computational and real-time constraints. For practical engineering implementation, G_{FC} should be simplified.

Considering that the dominant harmonic components in the grid voltage are typically the 3rd, 5th, ..., and 25th-order

harmonics, the simplified controller should retain similar frequency-domain characteristics at these specific harmonic frequencies. According to (18), the Bode diagram of the original G_{FC} is shown in Fig. 8. The magnitude slope of G_{FC} is approximately 20 dB/dec, and its phase remains close to 90° within the frequency range of 150 Hz to 1250 Hz. These frequency-domain characteristics indicate that G_{FC} behaves similarly to an integrator over the harmonic frequency range. To facilitate practical implementation, the feedforward controller is simplified as an integrator. Its discrete-domain transfer function is given as

$$G'_{FC}(z)=\frac{2K_{FC}(z-1)}{T_{sa}(z+1)} \tag{20}$$

where K_{FC} is the gain of the simplified feedforward controller. Since the magnitude of G_{FC} at 150Hz is −42.2dB, K_{FC} is derived as 8.24×10^{-6}.

The Bode diagram of the simplified feedforward controller is also shown in Fig. 8. Its magnitude and phase responses closely match those of G_{FC} at the dominant harmonic frequencies of the grid voltage. As a result, the simplified controller retains the desired harmonic rejection capability while being suitable for DSP implementation, thereby offering enhanced practicality.

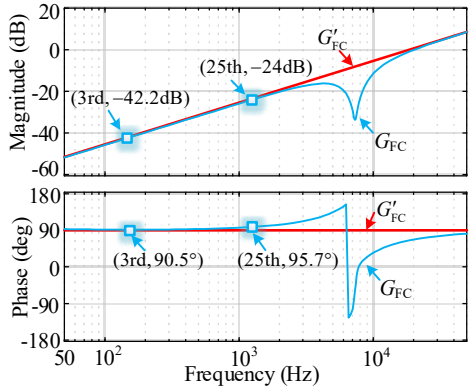

Fig. 8. Bode diagrams of G_{FC} and G'_{FC}.

C. Performance Analysis and Parameter Design of PR-ILC

In this section, the stability and harmonic suppression characteristics of the proposed closed-loop control system based on the PR-ILC are analyzed. On this basis, the parameter design of the PR-ILC is presented.

First, the stability of the proposed closed-loop control system is analyzed. As the feedforward control branch does not affect system stability, it is excluded from the analysis. According to Fig. 7, the structure of the closed-loop control system is shown in Fig. 9.

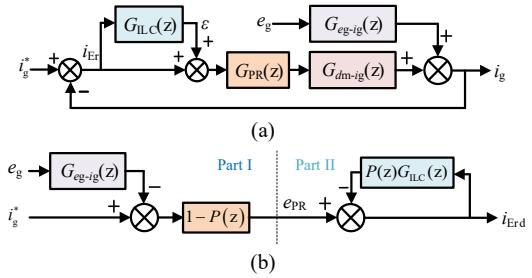

Fig. 9. Block diagram of proposed closed-loop control strategy. (a) Control structure. (b) Equivalent structure.

From Fig. 9(a), the stability is co-determined by the PR controller and ILC. The dynamic coupling between these two controllers complicates their independent parameter tuning. To facilitate the design of the composite controller, the current tracking error i_{Er} is analyzed in detail.

According to Fig. 9(a), i_{Er} is derived as

$$i_{Er}(z)=\frac{i_g^*(z)-G_{eg-ig}(z)e_g(z)}{1+\left[1+G_{ILC}(z)\right]G_{PR}(z)G_{dm-ig}(z)} \tag{21}$$

The transfer function of the closed-loop control system with only the PR controller is expressed as

$$P(z)=\frac{G_{PR}(z)G_{dm-ig}(z)}{1+G_{PR}(z)G_{dm-ig}(z)} \tag{22}$$

According to (21) and (22), the current control error is derived as

$$i_{Er}(z)=\frac{\left[1-P(z)\right]\left[i_g^*(z)-G_{eg-ig}(z)e_g(z)\right]}{1+P(z)G_{ILC}(z)} \tag{23}$$

Based on (23), the control block diagram is equivalently represented in the equivalent configuration depicted in Fig. 9(b). The overall system stability depends on two subsystems, and the system is stable only if both satisfy their respective stability criteria. According to classical control theory, these criteria are defined as follows:

Part I: The closed-loop transfer function $P(z)$, considering only the PR controller, must be stable. Specifically, the phase margin of $G_{PR}(z)G_{dm\text{-}ig}(z)$ should exceed 45°.

Part II: The phase margin of $G_{ILC}(z)P(z)$ should exceed 45°.

From these criteria, the design of the PR controller parameters is independent of the ILC, whereas the ILC design depends on the PR controller. Therefore, the PR controller parameters are designed first to ensure the stability of Part I. Then, $P(z)$ is obtained and used as the plant for the ILC parameter design. Based on these theories, the controller parameters will be designed.

From Fig. 9(a), the controlled objective is $G_{dm\text{-}ig}(z)$. Based on the built model in Section II, the transfer function $G_{dm\text{-}ig}(s)$ in the continuous domain is obtained from (12). However, the proposed control strategy is implemented on a DSP platform, and it operates in the discrete-time domain. To bridge this domain gap, the Tustin transformation is adopted, and the transfer function of the control object in the discrete domain is obtained as

$$G_{dm-ig}(z)=G_{dm-ig}(s)\Big|_{s=\frac{2}{T_s}\frac{1-z^{-1}}{1+z^{-1}}}$$

$$=\frac{\sqrt{2}I_{s\_r}\cos\left(\pi D_{m\_r}/2\right)+2U_{c\_r}\sin\left(\pi D_{m\_r}\right)G_{Ucd-Is}(z)/\pi}{1+\left[\frac{2(z-1)L_g}{T_{sa}(z+1)}+R_g\right]\left[\frac{2(z-1)C_g}{T_{sa}(z+1)}+\frac{8G_{Ucd-Is}(z)}{\pi^2}\sin^2\left(\frac{\pi}{2}D_{m\_r}\right)\right]} \tag{24}$$

Based on (24), the PR controller parameters are designed first. According to the classical control theory, the desired phase margin is greater than 45° to ensure stability. The desired cutoff frequency is set to 500 Hz, which is one-tenth of the grid-side LC filter's cutoff frequency, to avoid oscillations caused by the filter. Additionally, the magnitude gain at 50 Hz should exceed 40 dB to achieve the zero steady-state error tracking for the desired fundamental grid current. Accordingly, the parameters of the PR controller in

(15) are designed as K_p=0.2, K_r=43, ω_c=2 rad/s, and ω_1=100π rad/s. Fig. 10 shows the Nyquist curve of $G_{PR}(z)G_{dm\text{-}ig}(z)$. The phase margin is approximately 48°, confirming the stability of the closed-loop system with only the PR controller.

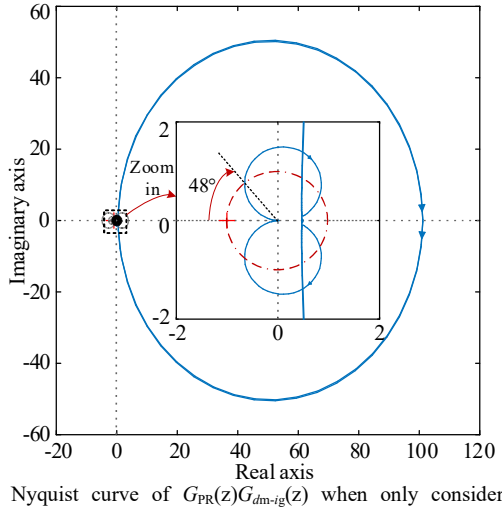

Fig. 10. Nyquist curve of $G_{PR}(z)G_{dm\text{-}ig}(z)$ when only considering PR controller.

After designing the PR controller parameters, the closed-loop transfer function $P(z)$, considering only the PR controller, is obtained from (22), and the ILC parameters are then designed. Prior to the design, the effects of the ILC parameters on system stability and harmonic suppression capability are analyzed.

According to the stability criteria of Part II, the Nyquist curves of $G_{ILC}(z)P(z)$ under different ILC parameters are plotted in Fig. 11. In Fig. 11(a), Λ is constant, and γ and ζ vary from 0.3 to 0.9. As γ and ζ increase, the magnitude of $G_{ILC}(z)P(z)$ grows larger, pushing the system toward instability. When γ and ζ exceed 0.7, the Nyquist curve encircles the $(-1, j0)$ point in the complex plane, resulting in an unstable closed-loop control system. In Fig. 11(b), γ and ζ are constant, and Λ varies from 0.1 to 0.9. Within the variation range of Λ, the Nyquist curve does not encircle the $(-1, j0)$ point in the complex plane. This indicates that Λ has minimal effect on system stability.

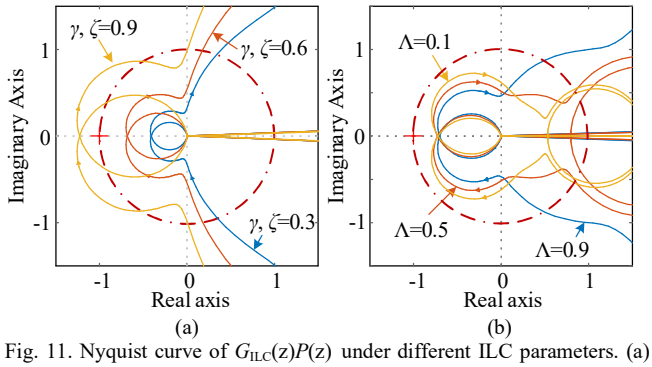

Fig. 11. Nyquist curve of $G_{ILC}(z)P(z)$ under different ILC parameters. (a) Variation with γ and ζ. (b) Variation with Λ.

Subsequently, the effect of the ILC parameters on harmonic suppression capability is researched. To characterize this capability, the transfer function $G_{eg\text{-}iEr}$, representing the relationship between grid voltage and current control error, is analyzed. From (21), $G_{eg\text{-}iEr}$ is derived as

$$G_{eg-iEr}(z)=\frac{i_{Er}(z)}{e_g(z)}=\frac{-G_{eg-ig}(z)}{1+\left[1+G_{ILC}(z)\right]G_{PR}(z)G_{dm-ig}(z)} \quad (25)$$

Based on (25), the amplitude-frequency characteristic of $G_{eg\text{-}iEr}$ under different ILC parameters is shown in Fig. 12. The control error decreases with increasing γ and ζ, and with decreasing Λ. This indicates that the harmonic suppression capability of the PR-ILC improves as γ and ζ increase and Λ decreases. To achieve a trade-off between system stability and harmonic suppression performance, the optimized parameters are selected as γ=ζ=0.6 and Λ=0.1.

Compared to the standalone PR controller, the proposed PR-ILC significantly reduces the current control error at harmonic frequencies, thereby validating its enhanced harmonic suppression performance.

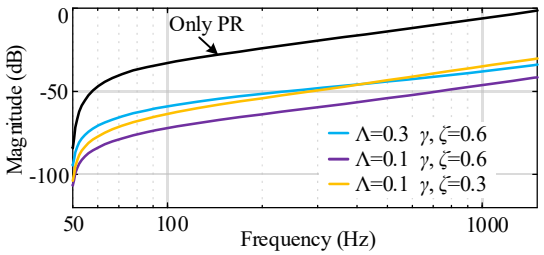

Fig. 12. Amplitude-frequency characteristic of current control error under proposed PR-ILC with different parameters.

The relationship between key controller parameters (K_p, K_r, γ, ζ, Λ) and system performance in terms of phase margin and grid current THD is shown in Table I. The table enables readers to quickly observe how changes in controller parameters influence the system's phase margin and harmonic suppression.

TABLE I RELATIONSHIP BETWEEN CONTROLLER PARAMETER AND SYSTEM PERFORMANCE

K_p	K_r	γ	ζ	Λ	Phase margin	THD
		0.9	0.9	0.1	-8°	/
		0.6	0.6	0.1	32°	1.24%
0.2	43	0.3	0.3	0.1	42°	2.55%
		0.6	0.6	0.3	39°	2.31%
		0.6	0.6	0.5	47°	3.26%

V. EXPERIMENTAL VERIFICATION

To validate the effectiveness of the proposed closed-loop control strategy, an experimental platform for the MC-based WPT system is established, as shown in Fig. 13. A programmable AC source is employed to emulate the grid, while a DC power supply simulates the EV battery. The digital controller is implemented on a TMS320F28377S DSP. The key experimental parameters are summarized in Table II. To replicate the grid harmonic conditions, the AC source is configured to inject harmonic components into the grid voltage. Specifically, 10% 3rd, 5% 5th, and 5% 7th harmonics are introduced into the output voltage, thereby enabling the evaluation of harmonic suppression performance under distorted grid scenarios.

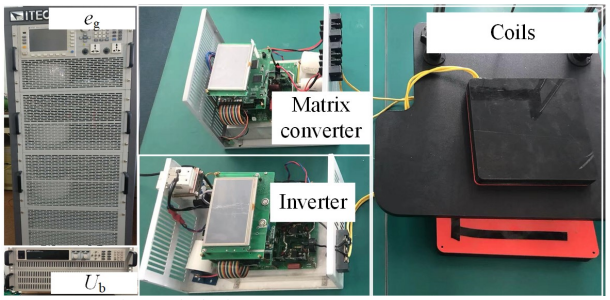

Fig. 13. Experimental platform.

TABLE II MAIN EXPERIMENTAL PARAMETERS

Parameter	Value	Parameter	Value
Output power	500 W	M	23 μH
Grid fundamental voltage	110 V_{RMS}	C_p	20.6 nF
Input DC voltage U_b	100 V	C_s	35 nF
f_s	85 kHz	L_g	50 μH
L_p	170 μH	C_g	20 μF
L_s	100 μH		

The experimental waveforms under the PR controller alone are shown in Fig. 14. Fig. 14(a) and (b) show the steady-state waveforms and fast Fourier transform (FFT) results under the ideal grid voltage condition. The grid current amplitude reaches 6.5 A, with a THD of 1.08%. These results demonstrate accurate zero steady-state error tracking of the fundamental component and validate the successful realization of V2G operation in the MC-based WPT system.

Fig. 14(c) and (d) show the experimental results under distorted grid voltage conditions. The significant distortion is observed in the grid current, primarily comprising 4.4% 3rd-harmonic, 3.6% 5th-harmonic, and 3.8% 7th-harmonic components. The dominant harmonic orders directly correspond to the injected grid voltage harmonics. The THD of the grid current reaches 7.16%, exceeding the IEEE 519-2014 limit of 5%. These results indicate that although the conventional PR controller ensures zero steady-state error tracking of the fundamental current, it cannot suppress harmonic distortions caused by non-ideal grid conditions.

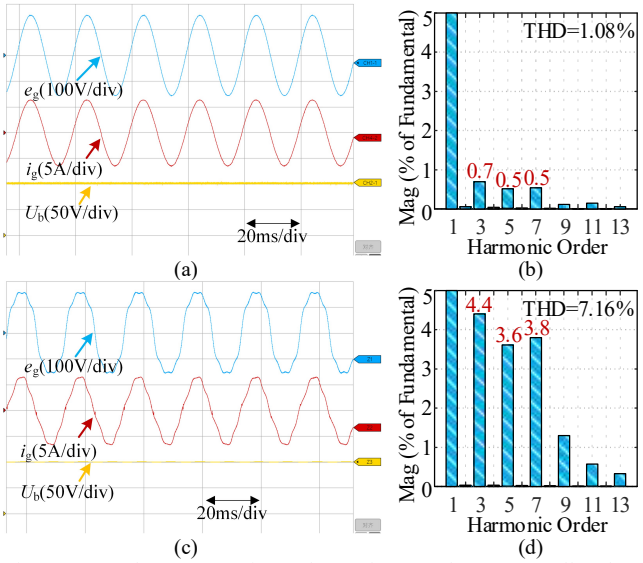

Fig. 14. Steady-state experimental waveforms under PR controller alone. (a) Waveforms under ideal grid voltage. (b) FFT of grid current under ideal grid voltage. (c) Waveforms under grid voltage harmonics. (d) FFT of grid current under grid voltage harmonics.

Fig. 15 shows the experimental waveforms of the proposed control strategy applied to the MC-based WPT system. Fig. 15(a) and (b) present the experimental results under the proposed composite control architecture integrating feedforward control + PR control without ILC. The grid current distortion is significantly mitigated, with the 3rd, 5th, and 7th harmonic components reduced to 1.7%, 0.9%, and 2.2%, respectively. As a result, the grid current THD decreases to 3.52%. Although the feedforward control effectively compensates for grid voltage harmonics, it cannot fully suppress them in practical systems. The discretization errors at lower sampling frequencies and parameter mismatches, such as coil displacement affecting inductance, further limit the feedforward control performance in harmonic compensation.

Fig. 15(c) and (d) show the results under the PR-ILC-based closed-loop controller alone, without feedforward compensation. The 3rd, 5th, and 7th harmonic components are 1.8%, 1.2%, and 1.1%, respectively, and the THD is 2.61%. These results confirm that both the feedforward control architecture and the PR-ILC independently provide effective harmonic suppression, each ensuring compliance with grid standards.

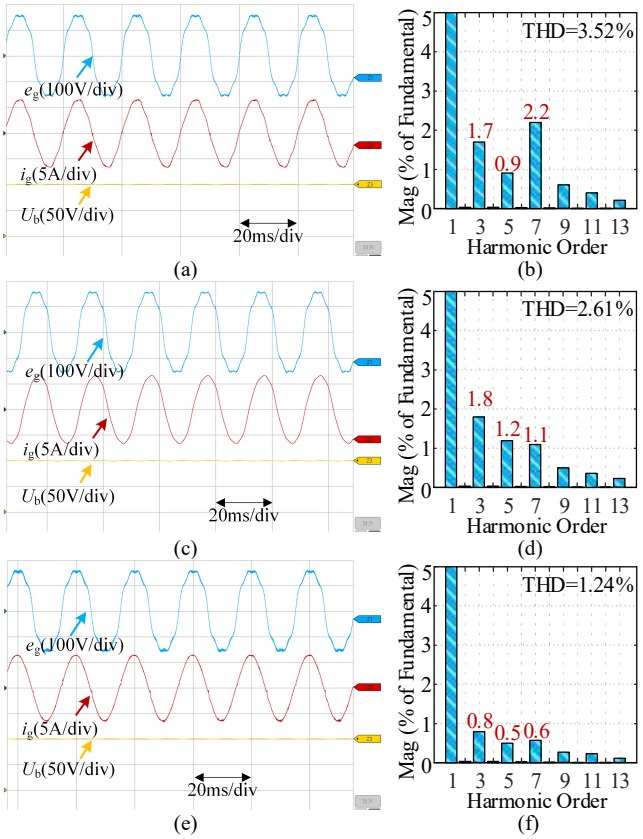

Fig. 15. Steady-state experimental waveforms under proposed control strategy. (a) Waveforms under feedforward control + PR control without ILC. (b) FFT of grid current under feedforward control + PR control without ILC. (b) FFT of grid current under PR-ILC. (e) Waveforms under feedforward control + PR-ILC. (f) FFT of grid current under feedforward control + PR-ILC.

Further, the proposed feedforward control architecture and PR-ILC-based closed-loop controller are both implemented, with corresponding waveforms depicted in Fig. 15(e) and (f). The 3rd, 5th, and 7th harmonic components are further reduced to 0.8%, 0.5%, and 0.6%,

and the THD is significantly reduced to 1.24%. This synergistic control approach outperforms either method alone, achieving a substantial improvement in grid current quality. Compared to the conventional PR control, which yields a THD of 7.16%, the proposed strategy achieves a marked reduction to 1.24%, effectively eliminating the adverse impact of grid voltage harmonics on the grid current waveform.

To verify the transient performances of the MC-based WPT system under the proposed control strategy, the transient experimental waveforms under different operation conditions are shown in Fig. 16~Fig. 18. Fig. 16 shows the waveforms when the closed-loop reference of grid current amplitude steps from 4 A to 6.5 A and from 6.5 A to 4 A, respectively. The grid current exhibits fast and accurate tracking, with a transient response time of less than 2 ms. Fig. 17 shows the waveforms when the grid voltage amplitude steps up from 124 V to 155 V and down from 155 V to 124 V. Fig. 18 shows the waveforms when the input DC voltage U_b varies from 100 V to 120 V and from 120 V to 100 V. In both cases, the grid current maintains stable and highly sinusoidal waveforms. This validates that the proposed control strategy ensures the system stability and superior steady-state and transient performance across diverse operation conditions.

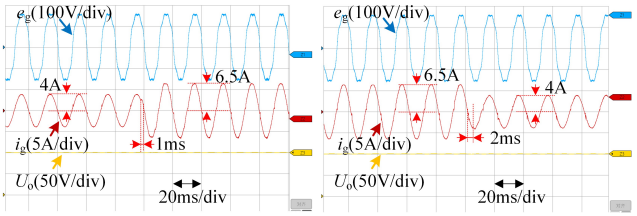

(a) (b)

Fig. 16. Experimental waveforms with stepping of grid current reference. (a) From 4 A to 6.5 A. (b) From 6.5 A to 4 A.

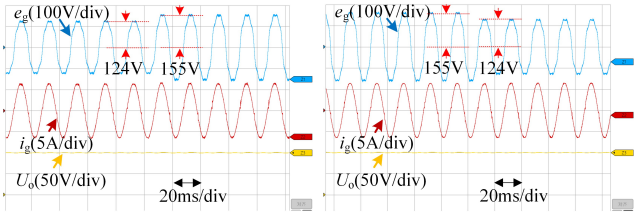

(a) (b)

Fig. 17. Experimental waveforms with variation of grid voltage. (a) From 124 V to 155 V. (b) From 155 V to 124 V.

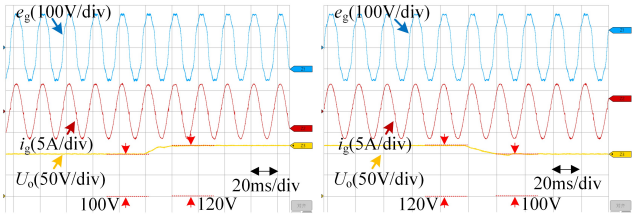

(a) (b)

Fig. 18. Experimental waveforms with variation of input DC voltage. (a) From 100 V to 120 V. (b) From 120 V to 100 V.

To verify the ride-through capability under grid-fault conditions, the experimental waveforms under a 50% grid-voltage sag lasting 20 ms are shown in Fig. 19. The grid current remains smooth during the voltage sag, with virtually no oscillations, overshoot, or other undesirable transient behaviors. These results confirm that the proposed FC + PR-ILC control strategy not only achieves effective harmonic suppression but also maintains stable operation and fast recovery under dynamic grid-voltage disturbances, thereby further validating its robustness and practical applicability.

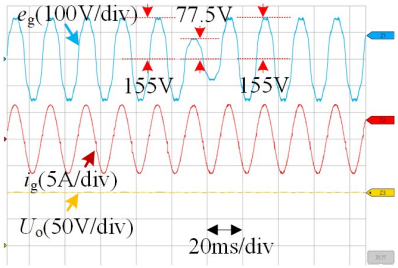

Fig. 19. Experimental waveforms under a 50% grid-voltage sag lasting 20 ms with proposed FC + PR-ILC control strategy.

Finally, the grid current THD under various load conditions is compared, as shown in Fig. 20. Across the entire load range, the proposed FC + PR-ILC control strategy consistently outperforms both the feedforward control and PR-ILC strategies when applied individually. All proposed methods exhibit better performance than the conventional PR control. Moreover, the proposed control strategy ensures that the grid current THD remains within the limits specified by grid standards under all tested load conditions, demonstrating its robustness and effectiveness in maintaining power quality across varying operational scenarios.

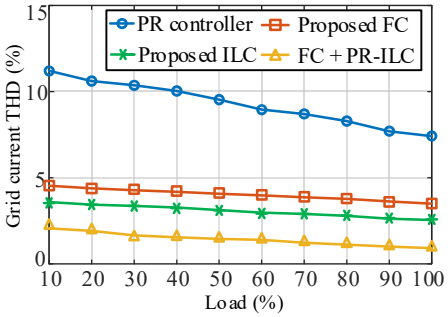

Fig. 20. Comparison of grid current THD under different load conditions.

The experimental results under variations in mutual inductance, self-inductance, and resonant capacitance are shown in Fig. 21. The FC + PR control strategy exhibits a significant increase in THD with parameter changes. However, the PR-ILC effectively compensates for these variations, ensuring robust harmonic suppression. With the FC + PR-ILC strategy, THD consistently remains below 2%, outperforming the other strategies. This confirms that effective harmonic suppression is maintained even under substantial parameter variations and coil misalignment, demonstrating the strong robustness and generalization capability of the proposed FC + PR-ILC control strategy.

Table III provides a comparison across different methods. The proposed FC + PR-ILC strategy achieves the lowest grid current THD while keeping DSP and memory costs at a moderate level, demonstrating trade-offs of performance and complexity.

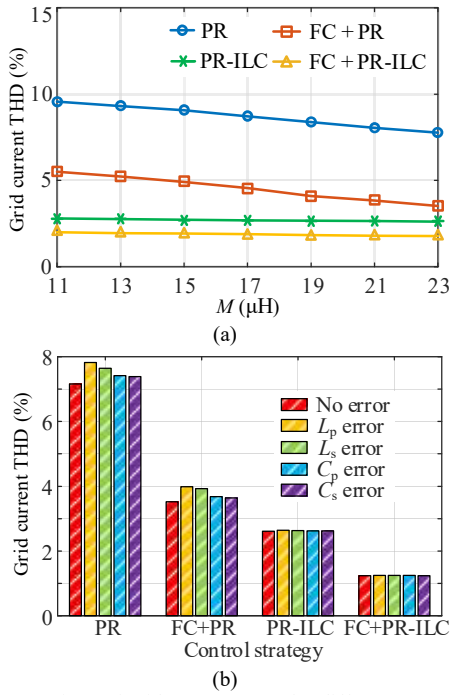

Fig. 21. Comparison of grid current THD for different control strategies under parameter variations. (a) Mutual inductance variation. (b) Inductance and capacitance variation.

TABLE III COMPARISON OF COMPUTATIONAL BURDEN AND PERFORMANCE OF DIFFERENT CONTROL STRATEGIES

Control strategies	Current THD	Transient time	DSP computational time	Memory footprint
Conventional PR [25]	7.16%	<10 ms	115 ns	28 Bytes
Multiple PR [24]	2.89%	<10 ms	575 ns	140 Bytes
FC + PR	3.52%	<10 ms	160 ns	44 Bytes
PR-ILC	2.61%	<10 ms	170 ns	52 Bytes
FC + PR-ILC	1.24%	<10 ms	215 ns	68 Bytes

VI. CONCLUSION

In this paper, the linearized model of the MC-based WPT system under V2G operation is built, revealing that the grid voltage harmonics induce severe current distortion. On this basis, a composite control architecture integrating grid voltage feedforward compensation and grid current closed-loop regulation is proposed. Furthermore, a PR-ILC-based closed-loop controller is developed to enhance harmonic suppression performance. Both strategies demonstrate effective harmonic mitigation individually, while their synergistic integration achieves a substantial reduction in grid current THD. The proposed method is crucial for the practical V2G application of the MC-based WPT system. It also offers broad applicability to other V2G-enabled systems requiring high power quality.

REFERENCES

[1] W. Liu, K.T. Chau, X. Tian, H. Wang and Z. Hua, "Smart wireless power transfer – Opportunities and challenges," *Renew. Sustain. Energy Rev.*, vol. 180, no. 113298, pp. 1-22, Jul. 2023.

[2] Y. Wang, H. Liu, H. Yu and P. Wheeler, "A battery wireless charger with full load range soft-switching operation and zero-switching-loss inverter," *IEEE Trans. Ind. Electron.*, vol. 71, no. 7, pp. 7063-7074, Jul. 2024.

[3] Y. Wei and F. Wu, "Indirect control strategy of secondary current for LCC-series compensated wireless power transfer system based on primary current closed-loop control," *IEEE Trans. Transp. Electr.*, vol. 8, no. 2, pp. 1553-1565, Jun. 2022.

[4] K.T. Chau, "Pure electric vehicles," *Alternative Fuels and Advanced Vehicle Technologies for Improved Environmental Performance – Towards Zero Carbon Transportation*, R. Folkson, Ed. Cambridge, UK: Woodhead Publishing, 2014, pp. 655–684.

[5] W. Liu, J. Lu, C.C. Mi and K.T. Chau, "Integrated sensorless wireless charging using symmetric high-order network for multistorey car parks," *IEEE Trans. Power Electron.*, vol. 39, no. 8, pp. 10568-10581, Aug. 2024.

[6] J. Mai, A. Yang, Z. Liu, Y. Wang, B. Zhang and D. Xu, "A Segmented Parallel S/S Compensation Topology and Its Harmonic Suppression Method for IPT System," *IEEE J. Emerging Sel. Topics Power Electron.*, vol. 13, no. 4, pp. 4315-4325, Aug. 2025.

[7] Y. Wang, H. Liu, P. Wheeler and F. Wu. "Implementation and analysis of an efficient soft-switching battery wireless charger with re-configurable rectifier," *IEEE Trans. Ind. Electron.*, vol. 71, no. 5, pp. 4640-4651, May 2024.

[8] A. Triviño, I. Casaucao and M. Castilla, "Flexible regulation of active and reactive power for a fully controllable V2G wireless charger," *IEEE Trans. Transp. Electr.*, vol. 10, no. 1, pp. 1070-1079, Mar. 2024.

[9] C. Liu, K.T. Chau, D. Wu and S. Gao, "Opportunities and challenges of vehicle-to-home, vehicle-to-vehicle, and vehicle-to-grid technologies," *Proc. IEEE*, vol. 101, no. 11, pp. 2409-2427, Nov. 2013.

[10] A. Aktas, E. Aydin, O. C. Onar, G. -J. Su, B. Ozpineci and L. M. Tolbert, "Medium-duty delivery truck integrated bidirectional wireless power transfer system with grid and stationary energy storage system connectivity," *IEEE J. Emerging Sel. Topics Power Electron.*, vol. 12, no. 5, pp. 5364-5382, Oct. 2024.

[11] C. Yuan, B. Zou, Z. Huang, I. -W. Iam and C. -S. Lam, "Configuration and control design of inductive power transfer systems with back-end power factor correction," *IEEE J. Emerging Sel. Topics Power Electron.*, vol. 12, no. 5, pp. 5352-5363, Oct. 2024.

[12] Y. Wei, F. Wu, S. Wu and H. Liu, "Improved modulation strategy for three-phase matrix converter-based WPT system," *IEEE Trans. Transp. Electr.*, vol. 10, no. 2, pp. 3396-3406, Jun. 2024.

[13] A. Bala Naga Lingaiah and N. Reddy Tummuru, "A PV-utility integrated cascaded interleaved configuration-based IPT charging system for residential V2G and G2V applications of EV," *IEEE Trans. Transp. Electr.*, vol. 10, no. 3, pp. 6583-6595, Sept. 2024.

[14] R. P. Upputuri and B. Subudhi, "A comprehensive review and performance evaluation of bidirectional charger topologies for V2G/G2V operations in EV applications," *IEEE Trans. Transp. Electr.*, vol. 10, no. 1, pp. 583-595, Mar. 2024.

[15] L. Wang, U. K. Madawala and M. -C. Wong, "A wireless vehicle-to-grid-to-home power interface with an adaptive DC link," *IEEE J. Emerging Sel. Topics Power Electron.*, vol. 9, no. 2, pp. 2373-2383, Apr. 2021.

[16] F. Wu, Y. Wei, J. Su, K. Zhao and H. Liu, "Dual-side closed-loop control, stability analysis, and parameter design of two-stage LCC-LCC WPT," *IEEE J. Emerging Sel. Topics Power Electron.*, vol. 12, no. 1, pp. 305-315, Feb. 2024.

[17] D. J. Thrimawithana and U. K. Madawala, "A novel matrix converter based bi-directional IPT power interface for V2G applications," *2010 IEEE International Energy Conference,* Manama, Bahrain, 2010, pp. 495-500.

[18] B. Vardani and N. R. Tummuru, "Bidirectional wireless power transfer using single phase matrix converter for electric vehicle application," *2019 IEEE Region 10 Conference (TENCON)*, Kochi, India, 2019, pp. 1523-1528.

[19] M. Moghaddami and A. I. Sarwat, "Single-phase soft-switched ac–ac matrix converter with power controller for bidirectional inductive power transfer systems," *IEEE Trans. Ind. Appl.*, vol. 54, no. 4, pp. 3760-3770, July-Aug. 2018.

[20] Y. Yang et al., "A monolithic bi-directional GaN/SiC hybrid field-effect transistor," *2024 36th International Symposium on Power Semiconductor Devices and ICs (ISPSD)*, Bremen, Germany, 2024, pp. 343-346.

[21] A. Garcia-Bediaga, A. Avila, I. Alzuguren, A. Sanchez and A. Rujas, "Power factor corrector control strategies of a bidirectional wireless battery charger with an unfolding active rectifier," *IEEE J. Emerging Sel. Topics Power Electron.*, vol. 11, no. 1, pp. 396-406, Feb. 2023.

[22] S. Weerasinghe, U. K. Madawala and D. J. Thrimawithana, "A matrix converter-based bidirectional contactless grid interface," *IEEE Trans. Power Electron.*, vol. 32, no. 3, pp. 1755-1766, Mar. 2017.
[23] J. Liu, F. Xu, C. Sun and K. H. Loo, "A soft-switched power-factor-corrected single-phase bidirectional AC–DC wireless power transfer converter with an integrated power stage," *IEEE Trans. Power Electron.*, vol. 37, no. 8, pp. 10029-10044, Aug. 2022.
[24] W. Wu, Y. Sun, M. Huang, X. Wang, H. Wang, F. Blaabjerg, M. Liserre and H. Chung, "A robust passive damping method for LLCL-filter-based grid-tied inverters to minimize the effect of grid harmonic voltages," *IEEE Trans. Power Electron.*, vol. 29, no. 7, pp. 3279-3289, Jul. 2014.
[25] Y. Wei, F. Wu, S. Wu and H. Liu, "Three-phase electrolytic-capacitor-less LCC-S WPT system with wide operation range," *IEEE Trans. Power Electron.*, vol. 39, no. 9, pp. 11803-11813, Sept. 2024.
[26] Z. U. Zahid et al., "Modeling and control of series-series compensated inductive power transfer system," *IEEE J. Emerging Sel. Topics Power Electron.*, vol. 3, no. 1, pp. 111-123, Mar. 2015.

Yuchen Wei received the B.S., M.S. and Ph.D. degrees in electrical engineering from Harbin Institute of Technology (HIT), China, in 2018, 2020 and 2024, respectively.

He is currently a Postdoctoral Fellow with the Department of Electrical and Electronic Engineering, The Hong Kong Polytechnic University, Hong Kong, China. His research interests include the areas of wireless power transfer technologies and power electronics and applications.

Wei Liu (Senior Member, IEEE) received the B.Eng. and M.Eng. degrees in electrical engineering from China University of Petroleum, Qingdao, China, and a Ph.D. degree in electrical and electronic engineering from The University of Hong Kong (HKU), Hong Kong, China, in 2014, 2017, and 2021, respectively.

He is currently an Assistant Professor at the Research Centre for Electric Vehicles and Department of Electrical and Electronic Engineering, The Hong Kong Polytechnic University (PolyU). He has also been an Honorary Assistant Professor at the Department of Electrical and Electronic Engineering, HKU, since 2023. Dr. Liu served as a Postdoctoral Fellow and was then promoted to a Research Assistant Professor from 2021 to 2023. He also worked as a Visiting Researcher with Nanyang Technological University, Singapore (NTU), in 2019. His research interests include electric vehicle technologies, wireless power transfer, power electronics, bioelectronics, and semiconductor devices.

Dr. Liu was the recipient of the Power Engineering Prize from HKU, two Gold Medals with Congratulations of the Jury in the International Exhibition of Inventions Geneva, the Second Place Prize Paper Award of *IEEE Journal of Emerging and Selected Topics in Power Electronics (JESTPE)*, the Excellent Paper Award, and the Best Presentation Award from international conferences in the area of Electric Vehicles and Transportation Electrification. He is also a Guest Associate Editor of *IEEE JESTPE*, Associate Editor of international journals, and Session Chair of international conferences.

Fengjiang Wu (Senior Member, IEEE) received the B.S., M.S. and Ph.D. degrees in electrical engineering from Harbin Institute of Technology (HIT), Harbin, China, in 2002, 2004 and 2007, respectively.

Since 2007, he has been with the Department of Electrical Engineering, HIT, where he is currently a full Professor. He has published more than 100 top-tier journal papers.

His research interests include the area of renewable energy generation, energy storage systems, wireless power transfer, solid state transformer and microgrid. Prof. Wu serves as the Associate Editors of IEEE Access and IET Power Electronics.

Chang Liu received the B. Eng degree in Electrical Engineering and Automation from Harbin Institute of Technology, Harbin, China, in 2021, and the M.Phil degree in Sustainability and Environment from the Hong Kong University of Science and Technology, Guangzhou, China, in 2024.

He is currently working towards the Ph.D degree at the Hong Kong Polytechnic University. His research interests include electric vehicles and wireless power transfer related technologies.

K. T. Chau (Fellow, IEEE) received the B.Sc. (Eng.), M.Phil., and Ph.D. degrees in electrical and electronic engineering from The University of Hong Kong, Hong Kong, in 1988, 1991, and 1993, respectively. Currently, he serves as Chair Professor of Electrical Energy Engineering at the Department of Electrical and Electronic Engineering and Co-Director at the Research Centre for Electric Vehicles, The Hong Kong Polytechnic University. His research interests include electric and hybrid vehicles, power electronics and drives, and renewable energies. He is the author of nine books and more than 400 journal papers.

Prof. Chau is a Fellow of the Institution of Engineering and Technology (IET), U.K., and of the Hong Kong Institution of Engineers. He is a Chartered Engineer. He was the recipient of the Changjiang Chair Professorship from the Ministry of Education, China, and the Environmental Excellence in Transportation Award for Education, Training, and Public Awareness from the Society of Automotive Engineers International.